Improve on Dual-Energy protocol for rock characterization and monitoring of porosity and phase saturations during multiphase flow

Janeth A. Vidal Vargas[1*], *Walter L. F.* Antelo[1], and *Rosangela B. Z. L.* Moreno[1]

[1]FEM-UNICAMP, Av. Antonio da Costa Santos, 73 - Cidade Universitária, Campinas - SP, 13083-890, Brazil

Abstract. Computed tomography (CT) is widely used in the petroleum industry as a non-destructive technique for rock petrophysical characterization. X-ray tomography applied during multiphase flow throughout porous media helps to understand rock heterogeneities and flow dynamics. The CT image quality depends on the combination of acquisition parameters and image reconstruction algorithms (kernels). The main CT scan acquisition parameters are energy level (kV), X-ray tube current (mA), slice thickness, FOV, and voxel size. Convolution kernels depend on the characteristics of the sample being scanned. Based on these parameters, Dual-Energy and Single-Energy CT scans were applied to obtain the effective porosity, and fluid saturations related with absolute and effective permeabilities. Analysing the images quality and comparing all the results, we were able to point out the best kernel among those used and discuss the applicability of the studied CT protocols and procedures to evaluate dry and saturated rock samples. This study can be very useful for the evaluation of heterogeneous porous media through X-ray image acquisitions.

1 Introduction

The petroleum industry has widely applied X-Ray computed tomography (CT) in hydrocarbon exploration to evaluate the spatial distribution of the petrophysical properties of reservoir rocks. This non-destructive technique allows the possibility of quantifying internal structures based on the measurement of X-ray attenuation coefficients, which depend on the physical and chemical properties of the analyzed materials. Therefore, computed tomography provides qualitative analysis and can be used to obtain quantitative information such as bulk density, porosity, and fluid saturation. These parameters measured from CT images highly depend on image quality [1,2,3,4].

A compromise between spatial resolution and sample size limits the quantification and characterization of the porous structures, pushing the combination between low- and high-resolution techniques [5]. There is a critical need to obtain data at the pore scale, which is crucial to characterize the recovery mechanisms influencing the fluid flow through complex and heterogeneous porous media, such as carbonate rocks. Thus, the Medical-CT scan technique is complemented with micro-CT and synchrotron systems that allow access from a few nanometer spatial resolutions to rock-fluid and fluid-fluid interactions at the pore-particle scale. However, it is essential to note that image analysis is time-consuming. Despite developing techniques for heterogeneous systems characterization on the micro and nanoscale, process optimization must be applied to fractured or dolomitized carbonates, on the macro scale [4,6].

Larmagnat et al. (2019) [4] improved the method for evaluating porosity distribution using Medical-CT scans on heterogeneous, fractured, or dolomitized carbonate reservoir rocks. They developed a low-cost and easy-to-operate coreflooding system where multiple samples can be scanned simultaneously. The methodology tested on a set of rock samples showed a strong correlation between conventional gas porosimetry measurements and porosity determined by computed tomography. Using Dual-Energy computed tomography (DECT) to evaluate reservoir rocks involves scanning the rock twice. The scan is performed by applying a different X-ray energy each time. Wellington and Vinegar (1987) [2] stated that one image provides only the apparent density, and another provides the atomic number that can be obtained by scanning the sample at high (above 100 kV, Compton scattering dominant) and low (well below 100 kV, photoelectric absorption dominant) X-ray energies. Furthermore, Single- and Dual-Energy scanning has been used quite successfully in studies of multiphase flow visualization in porous media, where the spatial distribution of fluid saturation is difficult to achieve using conventional techniques [2,7,8].

When operating a CT scanner, the user must specify the acquisition and reconstruction parameters. The combination of the selected parameters results in an ideal protocol to produce an image with the quality necessary to provide the quantitative information required by the specific application. When the protocol changes, a CT scanner can map the same volume into slightly different CT numbers (CTN) [4,7]. Fitzhenry et al. 2022 developed a method for optimizing acquisition and reconstruction

* janeth@unicamp.br

parameters for applying computed tomography in multiphase flow [8]. Based on the above, this study aims to select the best reconstruction kernel for a given acquisition protocol to evaluate Dual- and SSingle-Energy porosity results, and the distribution of saturations during multiphase flow. In addition, the type of dopant and quantity was selected to prepare the synthetic seawater used in this study.

2 Materials and Methods

2.1 Rock Samples Handling and Basic Properties

Three outcrop rock samples were used to obtain the results preconized in this work. First, they were cleaned using a Soxhlet extraction system with toluene and methanol as solvents. Each solvent interacted with the sample for approximately eight hours. The stop criterion for toluene was visual, and the process was stopped as soon as the solvent was discolored. However, silver nitrate solution was used as an indicator of the presence of salts in methanol. After this cleaning process, the rocks are dried in an oven at 70 °C for 24 h. Following, gas porosity and gas permeability were measured using a gas porosimeter and permeability meter. Samples were assembled in a core holder with a confining pressure of 500 psi. The gas permeability values were corrected due to the Klinkenberg effect. Table 1 shows the basic properties obtained for the tested samples.

Table 1. Physical properties of Indiana Limestones (IL) outcrop samples

Properties	IL-3	IL-5	IL-12
Diameter (cm)	3.816	3.816	3.816
Length (cm)	30.06	30.06	30.05
Dry sample mass (g)	775.89	774.23	776.50
Bulk Volume (cm^3)	343.8	343.8	343.7
*Total Void Volume (cm^3)	66.5	64,0	65,0
**Dead Volume (cm^3)	11.66	11.66	11.66
Rock Void Volume (cm^3)	54.85	52.35	53.35
Gas Porosity (%)	16.0	15.2	15.5
Gas Permeability (mD)	150.1	171.2	167.5

*Total void volume refers all space void in the rock sample and any tubing connection in the flow path.

**Dead Volume is that portion of the void volume of any tubing connection in the flow path.

2.3 Characteristics of fluids

EMCA mineral oil and synthetic sea water (SSW) were used for the displacement test. The SSW composition was defined as presented by Clinckspoor et al. (2021) [9]. Table 2 shows the composition of the SSW and its pH, density, and ionic strength, calculated using the geochemical software PHREEQC.

2.4 Screening reconstruction protocol

Initially, the acquisition protocol designed for this study was used to screen available reconstruction kernels. Table 3 describes the acquisition and reconstruction parameters that were applied in the different stages of the work.

The screening of reconstruction protocols was carried out based on the methodology described by Völgyes et al. (2017) [10]. The reference materials are water and air, with a CT number (CTN) equal to 0 HU and -1000 HU, respectively. For image acquisition, the parameters described in Table 3 will be applied, and the fluids will be contained in an aluminum bottle (Figure 1a) and an acrylic bottle (Figure 1b), as seen in Figure 1. The images were analyzed using an image processing algorithm developed in Matlab by Vidal Vargas (2015) [11] and Avizo3D [12].

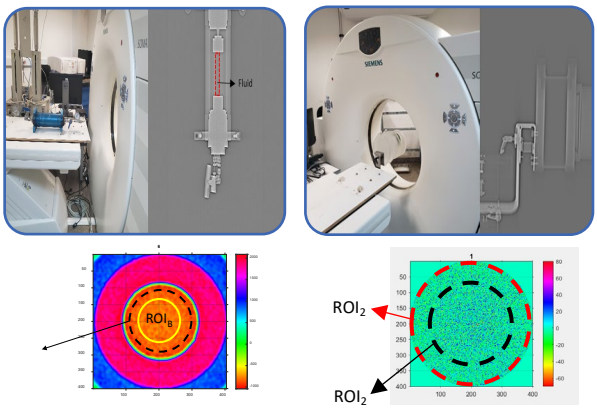

(a) (b)

Fig. 1. Experimental setup of screening reconstruction protocols a) Aluminum vessel and b) acrylic vessel.

Table 2. Composition of synthetic sea water (SSW).

Salts	Concentration		
	ppm	g/L	mol/L
KCl	749.3	0.7493	0.010051
$CaCl_2$:2H_2O	484.2	0.4842	0.003294
$MgCl_2$:6H_2O	1271.3	1.2713	0.006253
$SrCl_2$:6H_2O	5.2	0.0052	0.000020
$FeCl_3$:6H_2O	2	0.0020	0.000007
LiCl	1.2	0.0012	0.000028
NaBr	82.4	0.0824	0.000801
Na_2SO_4	57.7	0.0577	0.000406
NaCl	28251.3	28.2513	0.483401
pH	5.211		
ionic strength	0.5238		
density (g/ml)	1.0191		
TDS (mg/L)	30107.1		

Table 3. Acquisition and reconstruction parameters.

Acquisition Protocol			
Energy Level (kV)	130	110	80
X-ray Tube current (mA)	150	150	150
FOV(mm)	50	50	50

Slice thickness (mm)	0.75 and 1.0	0.75 and 1.0	0.75 and 1.0
Reconstruction Protocol			
Convolution kernel	B50s,B70s, B80s and U90s		

The contrast-to-noise ratio (CNR) was calculated to select the reconstruction protocol by applying the following equation:

$$CNR = \frac{2(S_A - S_B)^2}{\sigma_A^2 + \sigma_B^2} \quad (1)$$

where S_A and S_B are the mean values for signals with 2 ROIs, and σ_A^2 and σ_B^2 are the variances of those signals, respectively [10].

2.5 Porosity by Dual-Energy CT

The procedure for measuring porosity using Dual-Energy follows the methodology described by Siddiqui and Khamees (2004) [7], which suggests scanning three standard samples with known bulk density (ρ_b) to obtain the coefficients of the following equation:

$$m * CTN_{low} + p * CTN_{high} + q = \rho_b \quad (2)$$

where *m*, *p*, and *q* are Dual-Energy coefficients, CTN_{low} is the low energy CT number, CTN_{high} is the high energy CT number, and ρ_b is the bulk density.

After solving a system of three equations with three unknowns, the values of the coefficient m, p, and q will be obtained. With these values, ρ_b of the core samples can be determined by applying Eq. 3. Porosity can be calculated by applying the following equation:

$$\phi_{DE-CT} = \frac{\rho_{ma} - \rho_b}{\rho_{ma} - \rho_{fluid}} \quad (3)$$

where ρ_{fluid} is the fluid density, and ρ_{ma} is the matrix density and ρ_b is the bulk density of the core sample.

In this work, first, we performed an acquisition of Dual-Energy CT of standard material with known bulk density: Air, Water, Peek, PVC, Nylon, Quartz, and Aluminum. The acquisition and the reconstruction protocols are described in Table 3. Subsequently, samples IL-3, IL-5, and IL-12 were scanned.

The images obtained were analyzed using an image processing algorithm developed by Vidal Vargas (2015) [11] and Avizo3D [12]. Subsequently, three standards were chosen to obtain the *m*, *p*, and *q* values from Eq. 2. Them, the bulk density value of the three rock samples was determined. Finally, Eq. 3 was applied to calculate the porosity of each sample, considering different reconstruction protocols.

2.6 Select the amount and type of dopant for the brine

Different Synthetic Water (SW) formulations were made with different concentrations of dopant. The dopants used were Sodium Bromide (NaBr), Sodium Iodide (NaI), and Cesium Iodide (CsI). The new formulations were entered into the PHREEQC to determine the ionic strength, density, and pH. In PHREEQC, we adjust the amount of NaCl to keep the ionic strength of all solutions constant. The concentrations of dopants were 5%, 30%, and 60% of total salinity. The acquisition and reconstruction protocols applied are described in Table 3, according to the procedure of Fitzhenry et al. (2022) [8].

The experimental conditions for measuring CTN were 20 °C and 1450 psi. The fluids analyzed were sea water, EMCA, and brines doped with NaI, NaBr, and CsI in different concentrations (5 %, 30 %, and 60 %).

The first step of the analysis is to calculate, for each fluid, the ratios ($Ratio^{CT}$) between its CT numbers at high energy (CTN_{high}) and low energy (CTN_{low}) [8]:

$$Ratio^{CT} = \frac{CTN_{high}}{CTN_{low}} \quad (4)$$

$Ratio^{CT}$ values close to 1 indicate that the fluid in question is characterized by a slight difference in the CT number between two energy levels at which it is evaluated. Furthermore, different fluids with similar CT number energy dependencies will have similar $Ratio^{CT}$ values. The ability to reliably distinguish fluids requires the most significant possible difference in the energy dependence of the CT number of the two fluids, as represented by the Δ value:

$$\Delta = (Ratio_1^{CT} - Ratio_2^{CT})^2 \quad (5)$$

where $Ratio_1^{CT}$ is the $Ratio^{CT}$ of fluid 1, $Ratio_2^{CT}$ is the $Ratio^{CT}$ of fluid 2 and Δ is the difference between the CT ratios of fluids 1 and 2.

A matrix with the $\text{Ratio}_1^{\text{CT}}$ and Δ values results must be created to choose the high value of differentiation Δ, which represents the best acquisition parameters for evaluating phase saturations during multiphase flow.

2.7 Porosity and saturation measurement during two phase flow using Single-Energy technique

After determining the optimal reconstruction parameters, the concentration and doping agent were selected, and a brine injection and mineral oil injection were performed. The steps of the displacement experiment are following described. The experimental conditions were 1450 psi and 20 °C. The sample selected for the displacement test was IL-5. The sample was mounted in an aluminum core holder with a 6-pressure tap and 2500 psi confining pressure. A vacuum was applied to the sample for four hours. Initially, the sample was saturated with nitrogen (N_2) under the test conditions, and it was scanned using the acquisition protocol. The sample was vacuumed for four hours. Then, it was saturated with doped brine under the test conditions. Finally, absolute permeability

measurements were taken to the doped brine and a CT scan was carried out.

Using the results obtained from the methodology describetd above, the porosity profile of the sample can be calculated by applying the following equation:

$$\phi_{SE-CT} = \frac{CTN_{sat-brine} - CTN_{sat-N2}}{CTN_{brine} - CTN_{N2}} \quad (6)$$

where ϕ_{SE-CT} is the porosity of each slice in different positions of the rock sample, $CTN_{sat-brine}$ is the CT number of rock sample 100% saturated with brine, CTN_{sat-N2} is the CT number of rock sample 100% saturated with N_2, CTN_{brine} is the CT number of the brine and CTN_{N2} is the CT number of the N_2.

Afterwards, the mineral oil was injected until it reached the Swi, and a CT scan was carried out at injection times to monitor the oil advance front., Measurements of the effective oil permeability at Swi were carried out after the injection of 4 PVI. The next step was the injection of doped brine for 4PVI again. CT scans were also carried out at different injection times, and finally, the effective permeability to water at the S_{or} was measured. Subsequently, mineral oil was injected for 4PVI, CT scans were also conducted at different injection times. In the following step, the effective permeability of the oil in the S_{wi} was measured. Finally, saturations during injections were calculated based on the Equations (7) and (8).

$$S_{o,SE-CT} = \frac{1}{\phi_{SE-CT}} \left(\frac{CTN_{So} - CTN_{sat-brine}}{CTN_{oil} - CTN_{brine}} \right) \quad (7)$$

$$S_{w,SE-CT} = 1 - S_{o,SE-CT} \quad (8)$$

where ϕ_{SE-CT} is the porosity of each slice in different positions of the rock sample, $CTN_{sat-brine,i}$ is the CT number of rock sample 100% saturated with brine, $CTN_{So,SE-CT}$ is the CT number of rock sample with oil and brine, CTN_{brine} is the CT number of the brine, CTN_{Oil} is the CT number of the oil, $S_{o,SE-CT}$ is the saturation of oil each slice in different positions of the rock sample, and $S_{w,SE-CT}$ is the saturation of brine each slice in different positions of the rock sample.

Figure 2 shows the experimental setup used during the displacement test.

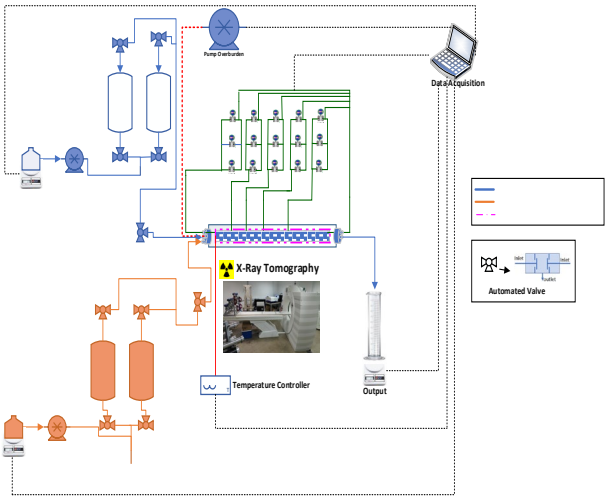

Fig. 2. Experimental setup for the core flooding tests

3 Results and Discussion

3.1 Select the best reconstruction protocol (Convolution Kernel)

For selecting the best reconstruction algorithm, tomography images were acquired from two standard fluids (water and air), at three different energy levels (130, 110, and 80kV), and using different reconstruction algorithms (convolution kernels: B50s, B60s, B70s, B75s, B80s, B90s, U90s and U91s). During image analysis, two regions of interest (ROI) were considered with a radius of 60 (ROI_B) and 100 (ROI_A), considering that the images have dimensions of 512x512 pixels. The CT numbers measured for water and air under different conditions present a difference of 120 to 280 HU about the reference value, which is a very high discrepancy if one considers the equipment tolerance of ±5HU. However, fluids (air and water) were measured in a dense aluminum vessel, contributing to poor image quality due to the artifact effect. The artifact generates a systematic discrepancy between the CTNs of the reconstructed image and the accurate attenuation coefficients of the object.

New image acquisition was performed using a sample holder to avoid interfere with validating the hypothesis regarding the presence of artifact and the selection of the B50s kernel. When analyzing the images, two regions of interest (ROI) with a radius of 200 (ROI_1) and 100 (ROI_2) were considered, considering that the images have a dimension of 512x512 pixels.

With the removal of the artifact effect on the CT numbers for air and water, the CNR was calculated again, and the values are presented in Table 4.

Table 4. CNR for Air and Water at Three Energy Levels and Different Convolution Kernels without Artifact.

CNR (Contrast-to-Noise Ratio)				
AIR				
Energy(kv)	**B50s**	**B70s**	**B80s**	**U90s**
130	15.02	17.00	15.91	20.42
110	0.40	0.17	0.29	0.21
80	2.82	2.52	1.74	2.43
WATER				
Energy (kv)	**B50s**	**B70s**	**B80s**	**U90s**
130	185.77	150.97	155.91	157.67
110	169.15	151.90	148.34	133.52
80	162.46	154.02	151.17	132.85

By removing the artifact effect from the CT number measurements and according to the choice criteria, defining a single kernel for the fluids and the different energy levels was unsuccessful. In the case of air, for 130kV, the best kernel is U90s; 110kV would be B50s, and for 80kV, it is B50s. However, for water, for 130kV, the best kernel is B50s, 110kV would be B60s, and for 80kV, it is B50s. Finally, it was decided to keep the B50s as the best kernel since, in the displacement tests in porous media, the images show an artifact effect due to the presence of the core holder.

3.2 Porosity measurement using the Dual-Energy technique

It was necessary to calculate the coefficients *m*, *p*, *q* from Eq. 2 to determine porosity using the Dual-Energy technique. To calculate those coefficients, the CT number (CTN of 7 standards of different materials at low (80kV) and high (130kV) energy levels were measured and recontructed (B50s, B70s, and B80s). The results obtained are presented in Table 5.

Table 5. Density, CTN_{Low} and CTN_{High} values for homogeneous standards.

*ID	ρ_b kg/m^3	CTN_{Low}		CTN_{High}	
		B50s	**B70s**	**B50s**	**B70s**
1	1.2922	-999.74	-999.72	-999.99	-999.98
2	1000	-2.034	-2.031	-2.088	-2.089
3	1305.4	160.85	151.41	188.85	177.84
4	1365.2	1033.4	1013.5	964.28	945.02
5	2153	1528.4	1501.6	992.27	972.05
6	2200	1559.8	1556.5	1275.9	1273.5
7	2704.6	2848.0	2760.8	2366.9	2297.7

*ID:1. Air, 2. Water, 3. Peek, 4. PVC, 5. Nylon, 6. Quartz, 7. Aluminum

To select the three standards to determine the *m*, *p*, and *q* coefficients, a graph of the CT number as a function of density was used to analyze the correlation coefficient (R^2) of the measurements obtained with CT-Scan and the density values. If the acquisition and reconstruction protocol is suitable for all patterns, R^2 will be very close to or equal to 1, and it will be possible to choose any pattern. However, if the pattern measurements were far from a linear correlation, choosing those closest to the linear relationship will be necessary. Figure 3 reflects the previous discussion applied for the reconstruction algorithm B50s.

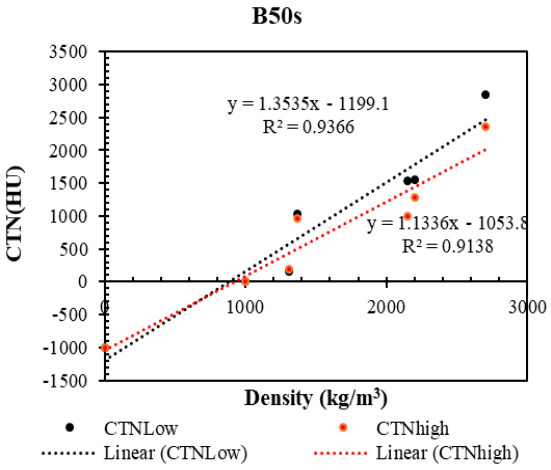

Fig. 3. CTN_{LOW} and CTN_{HIGH} as a function of density of the different standards applying the B50s kernel.

The R^2 coefficient for all kernels is of the same order of magnitude, but it can be seen that the peek, PVC, and nylon patterns are slightly outside the linear trend line. However, the different kernels' standards were air, water, and aluminum. Table 6 presents the results of the coefficients *m*, *p*, and *q* for the different reconstruction protocols.

By substituting the values of the coefficients *m*, *p*, and *q* in Eq. 2, it was possible to determine the bulk density of the rock samples IL-3, IL-5, and IL-12. Also, the densities of peek, PVC, nylon, and quartz were recalculated. A calibration curve was created for the density measured by computed tomography and the real densities of the different materials. Figure 4 presents the density calibration curve for the reconstruction algorithm B50s.

Table 6. Values of Dual-Energy coefficients for kernels B50s, B70s and B80s.

Coefficient	B50s	B70s	B80s
m	-1.3834	-1.2880	-1.2818
p	2.3840	2.2886	2.2823
q	1002.1629	1002.1635	1002.1601

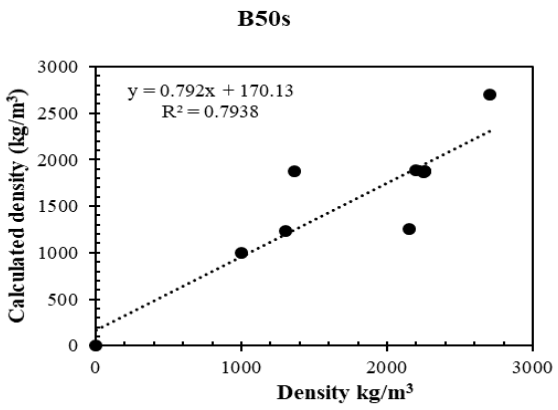

Fig. 4. Calculated density as a function of density of the different standards applying the B50s kernel.

The trend line correlation coefficient observed in Figure 4 presents a low fit quality. The leading cause of this discrepancy between measured and reference values is that the CT Scan acquisition and reconstruction parameters are inappropriate for the subjects analyzed. However, the CT Scan parameters would need adjustments to improve the calibration curve for different materials.

To calculate the average porosity and the porosity profile of the rocks (IL-3, IL-5, and IL-12) applying Eq. 3, the value of the matrix density (ρ_{ma}) is necessary. The ρ_{ma} value was determined considering that the Indiana Limestone rock comprises 98 % Calcite [13], so the ρ_{ma} is 2646 kg/m^3. Correcting the density by applying the calibration curves (Figure 4) is necessary to obtain the ρ_{maCT} value. The Table 7 presents the values of ρ_{ma}, ρ_{maCT} and the average porosities calculated with CT and the gas porosimeter.

Table 7 shows ϕ_{gas} is the effective porosity measured with the gas porosimeter. However, ϕ_{CT} is the total porosity measured using the Dual-Energy technique. By definition, the total porosity must be greater than the effective porosity, from which it can be concluded that the B50s kernel presents the most coherent values of total porosity. The effective porosity of the IL-5 sample is 15.23 %; however, the total porosity is 17.57 %, which means that the rock has 2.34% unconnected pores. Choosing the correct reconstruction algorithm allows for obtaining a total porosity value representative of the rock under study since if a different algorithm, such as B70s or B80s, had been chosen; the total porosity would be lower than the effective porosity.

Table 7. Density values of different materials for kernels B50s, B70s and B80s.

ID	ρ_{ma} (kg/m³)	ϕ_{gas} (%)	Kernels	ρ_{maCT} (kg/m³)	ϕ_{DE_CT} (%)
IL-3	2646	15.95	B50s	2265.76	17.43
			B70s	2310.55	16.08
			B80s	2313.37	16.00
IL-5	2646	15.23	B50s	2265.76	17.57
			B70s	2310.55	14.64
			B80s	2313.37	14.47
IL-12	2646	15.52	B50s	2265.76	17.31
			B70s	2310.55	14.38
			B80s	2313.37	14.20

Figure 5 and Figure 6 show the porosity profiles along the sample by applying the B50s, B70s, and B80s reconstruction algorithms to the IL-3 and IL-5, respectively. About B50s, the IL-5 rock shows a significant variation in porosity (14 % to 20 %) compared to the IL-3 sample, from which one can conclude the high heterogeneity of this rock. However, the porosity profile of rocks IL-3 shows zones with high porosity (16 % to 19 %) at the beginning of the sample and approximately in the middle of the sample. The B70s and B80s kernels present very similar porosity profiles with a slight difference in porosity across the sample.

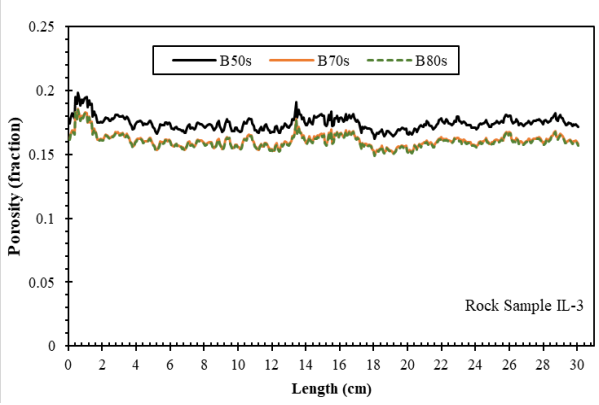

Fig. 5. Porosity profile for rock sample IL-3 applying the B50s, B70s and B80s convolution kernels.

3.3 Dopant screening

For the displacement test with more than one phase, the CT number of the different ones must be known to identify them in the computed tomography images and thus calculate the saturation of each phase. Furthermore, the phases must significantly differ in CT number to be distinguished. In the displacement test, brine and EMCA mineral oil were used. It was necessary to dope the brine to differentiate the phases with higher precision.

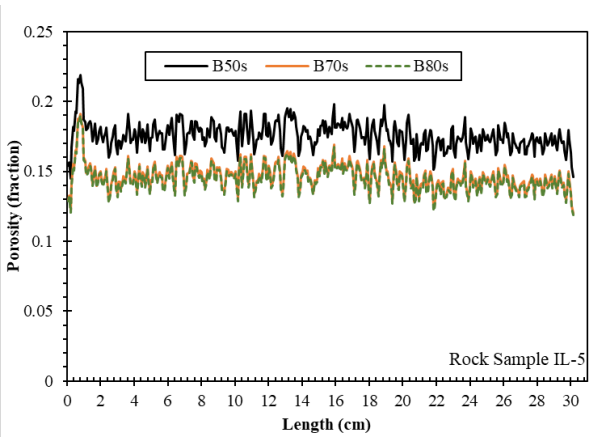

Fig. 6. Porosity profile for rock sample IL-5 applying the B50s, B70s and B80s convolution kernels.

The brine was doped with CsI, NaI, and NaBr in three different concentrations. The CT numbers of nitrogen, deionized water, brine without dopant, and EMCA mineral oil were also measured.

Figure 7 presents the results of fluids with an acquisition thickness of 0.75 mm and kV130kV. It can be seen that the CT numbers for the different fluids of the B70s, B80s, and U90s protocols show almost the same value. However, the B50s kernel presents different values. Brines doped with NaBr have lower attenuation values compared to CsI and NaI. At the lowest concentration, the difference is slight, but depending on the concentration, the difference between the dopants also increases.

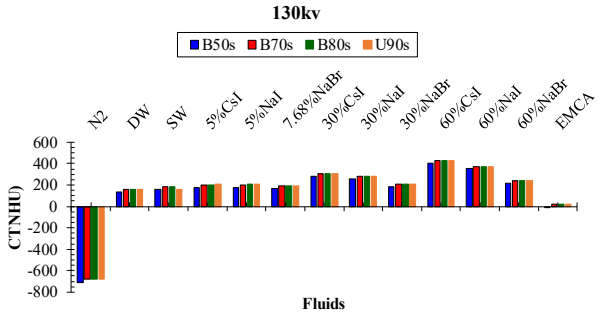

Fig. 7. Measured fluids CT number for different reconstruction protocols and slice thickness of 0.75 mm.

NaBr presents the smallest increase in attenuation about increasing concentration. It was observed that adding 5 % dopant generates a slight increase in the CTN, but still very close to the values of fluids without dopant. The difference between the CT numbers of NaI and CsI in all cases is approximately 7 %. Finally, the CsI dopant was chosen at a concentration of 30 % to perform the displacement test.

3.4 Acquisition and reconstruction parameters for multiphase flow

Based on the results of the dopant selection, the next step is to determine the ideal acquisition and reconstruction protocols applied in the X-ray computed tomography scan for multiphase flow. Table 8 and Table 9 present the decision matrix to determine the porosity and displacement test saturations, respectively.

Table 8 shows the $Ratio^{CT}$ (Eq. 4) results for the brine with 30 % CsI and nitrogen and Δ value between the two fluids. The $Ratio^{CT}$ values for each fluid are approximately the same in order of magnitude. It must be about the highest value to select the best combination of acquisition and reconstruction parameters Δ (Eq. 5), as it represents the difference in the CT number between the fluids. The higher the value of this parameter, the greater the ability to distinguish the fluids reliably. In the case of high energy, the parameter Δ shows values of approximately 0.21 for all reconstruction parameters, which are very close to the nitrogen. For the brine with 30 % CsI, any reconstruction kernel can be applied with the acquisition of high energy. The difference in the CT number of 30 % CsI and nitrogen is almost 1000 HU, which is why Δ presents high values in the different combinations of acquisition and reconstruction protocols.

Table 8. Matrix decision for selected the best acquisition and reconstruction protocols for the fluids designated for porosity measure.

CT Scan Parameters	$Ratio^{CT}_{30\%CsI}$	$Ratio^{CT}_{N_2}$	Δ
110 kV			
0.75mm B50s	0.713	1.028	0.099
0.75mm B70s	0.720	1.040	0.102
0.75mm B80s	0.720	1.040	0.102
0.75mm U90s	0.720	1.040	0.102
1mm B50s	0.711	1.030	0.102
1mm B70s	0.718	1.042	0.105
1mm B80s	0.718	1.042	0.105
1mm U90s	0.718	1.042	0.105
130 kV			
0.75mm B50s	0.601	1.050	0.201
0.75mm B70s	0.612	1.067	0.207
0.75mm B80s	0.612	1.067	0.207
0.75mm U90s	0.612	1.067	0.207
1mm B50s	0.599	1.052	0.205
1mm B70s	0.610	1.069	0.211
1mm B80s	0.610	1.069	0.211
1mm U90s	0.610	1.069	0.211

In the case of the displacement test, the phases involved are 30% CsI brine and EMCA mineral oil. Table 9 presents the main results of $Ratio^{CT}$ and Δ. The $Ratio^{CT}$ of the 30 % CsI brine is equal to 0.601 for the case of B50s and 0.612 for the kernels B70s, B80s, and U90s for the power of 130 kV, and in the case of 110 kV it is equal to 0.713 for the case of B50s and 0.720 for the B70s, B80s and U90s kernels, this is for 0.75mm acquisition; in the case of acquiring 1 mm, it presents similar values. In the case of 130 kV and 0.75 mm slice, the $Ratio^{CT}$ of EMCA mineral oil is equal to -0.831 for B50s, 0.339 for B70s, 0.338 for B80s and 0.342 for U90s; the 1mm slice values have approximately the same order of magnitude. The highest Δ value for the 30% CsI brine and the EMCA mineral oil was observed for kernel B50s for both the 0.75 mm and 1mm slices. Finally, based on Table 9, in the displacement test, 130 kV. Table 9 energy 0.75 mm slice and the B50s kernel will be applied to reconstruct the images.

Table 9. Matrix decision for selected the best acquisition and reconstruction protocols for the fluids designated for core flooding test.

CT Scan Parameters	$Ratio_{30\%CsI}^{CT}$	$Ratio_{EMCA}^{CT}$	Δ
110 kV			
0.75mm B50s	0.713	0.076	0.406
0.75mm B70s	0.720	0.613	0.012
0.75mm B80s	0.720	0.610	0.012
0.75mm U90s	0.720	0.617	0.011
1mm B50s	0.711	0.074	0.405
1mm B70s	0.718	0.619	0.010
1mm B80s	0.718	0.618	0.010
1mm U90s	0.718	0.618	0.010
130 kV			
0.75mm B50s	0.601	-0.831	2.050
0.75mm B70s	0.612	0.339	0.075
0.75mm B80s	0.612	0.338	0.075
0.75mm U90s	0.612	0.342	0.073
1mm B50s	0.599	-0.858	2.123
1mm B70s	0.610	0.335	0.075
1mm B80s	0.610	0.334	0.076
1mm U90s	0.610	0.338	0.074

3.5 Porosity measurement using Single-Energy technique

Applying Eq. 6, the porosity profile was calculated based on the sample saturated with nitrogen and brine at 30% CsI. Table 10 presents the porosity determined with the gas porosimeter, Dual-Energy technique, and the Single-Energy technique. The average effective porosity determined with the Single-Energy technique presents a value of 16.14 %, which, compared to the gas porosimeter measurement, has a difference of 5.97 %. The porosity measured by Dual-Energy technique represents the bulk porosity of the sample. Finally, the difference between bulk and effective porosity represents 1.43 %, representing the percentage of nonconnected pores in the porous medium.

Table 10. Different porosity measurements (B50s).

Sample	ϕ_{gas} (%)	ϕ_{SE-CT} (%)	ϕ_{DE-CT} (%)
IL-5	15.23	16.14	17.57

Figure 8 shows the porosity profile of the IL-5 sample obtained by Single and Dual-Energy applying the B50s reconstruction algorithm. The total porosity profile obtained with Dual-Energy (black curve) shows a high variation in porosity in the first 4 cm of the sample, ranging from 14 % to 21 %; subsequently, the porosity varies from 15 % to 19 % throughout the sample. The effective porosity profile obtained with Single-Energy presents smaller porosities with a porosity variation of 15 % to 17 % and a zone of high heterogeneity located from 11 to 19 cm. Finally, sample IL-5 is heterogeneous due to porosity changes throughout the sample.

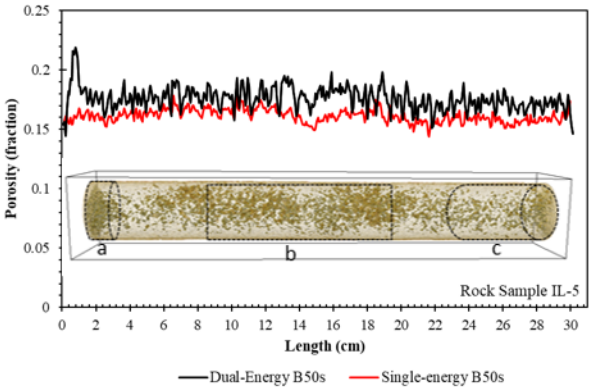

Fig. 8. Porosity profiles calculated by Dual- and Single-Energy techniques.

3.6 Saturation measurement during two phase flow using Single-Energy technique

Sample IL-5 has a porous volume of 55.46 ml, considering the porosity measured with X-ray computed tomography. After saturating the sample with 30%CsI brine, the first injection of Emca mineral oil was performed until irreducible water saturation (S_{wi}) was reached. 27 tomography acquisitions scans were performed at different injection times or injected pore volumes.

Table 11 shows the main results during the first oil injection process. The injection was carried out at different flow rates (0.3, 0.35, and 0.4 ml/min).

The IL-5 sample presents a S_{wi} equal to 0.54 after injecting 6.54 PVI of mineral oil. During the oil injection, water production was collected in a beaker, and it was possible to observe the production of approximately 24.34 ml of water until the injection of 1.50 VPI of Emca mineral oil, which would mean an oil saturation of 0.439. Finally, it is concluded that it was possible to obtain the same saturation values by applying CT analyses and mass balance.

Figure 9 shows the oil advance front during the oil injection process until reaching S_{wi}. After the injection of 0.45 PVI, the oil front reached the sample's end, representing the breakthrough point. The oil saturation profiles show an irregular shape of the advanced front, and the early breakthrough indicates the presence of a preferential path in the rock due to the heterogeneity already observed in the porosity profiles.

Table 11. Results of the first oil injection until reaching S_{wi}

N° SCAN	Pore Volume Injected (PVI)	$\bar{S}_o$	$\bar{S}_w$
CT1	0.05	0.032	0.968
CT2	0.12	0.071	0.929
CT3	0.16	0.106	0.894
CT4	0.19	0.141	0.859
CT5	0.23	0.175	0.825
CT6	0.26	0.210	0.790
CT7	0.30	0.250	0.750
CT8	0.34	0.285	0.715
CT9	0.38	0.323	0.677
CT10	0.41	0.359	0.641
CT11	0.45	0.395	0.605
CT12	0.49	0.415	0.585
CT13	0.53	0.421	0.579
CT14	0.54	0.422	0.578
CT15	0.56	0.424	0.576
CT16	0.58	0.427	0.573
CT17	0.62	0.431	0.569
CT18	0.83	0.416	0.584
CT19	0.89	0.417	0.583
CT20	0.95	0.423	0.577
CT21	0.97	0.424	0.576
CT22	1.01	0.425	0.575
CT23	1.10	0.427	0.573
CT24	1.20	0.434	0.566
CT25	1.28	0.433	0.567
CT26	1.50	0.438	0.562
CT_{Final}	6.54	0.460	0.540

After the first oil injection, sample IL-5 presented an oil saturation (S_o) of 0.46 and an irreducible water saturation (S_{wi}) of 0.54, which is the starting point for water injection. The flow rate varied from 0.12 to 0.3 ml/min during water flooding. The results of the water injection are summarized in Table 12. Twenty-one CT scans were run during the water injection, and 4.14 PVI were injected. The residual oil saturation (S_{or}) obtained after water injection was 0.308, representing a recovery of 33.0% of the initial oil. Furthermore, it can be observed that the breakthrough occurred after the injection of 0.17 PVI; that clearly shows the presence of a preferential path in the sample. From that moment onwards, the saturation change is minimal over time.

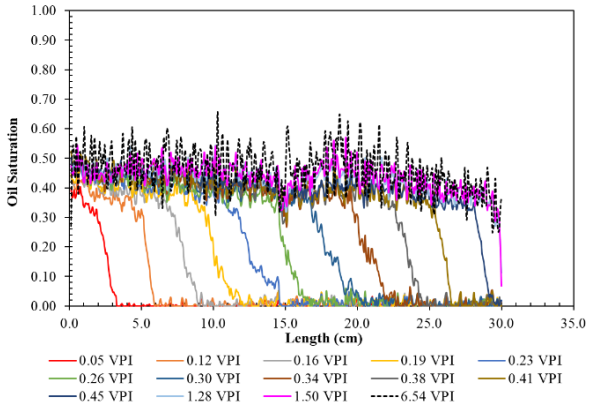

Fig. 9. Oil saturation profile during first oil injection until reaching Swi.

Figure 10 shows the water saturation profile throughout the sample until residual oil saturation is reached. In the water saturation profile, as a function of sample length, the water advance front can be observed until the breakthrough time is reached. The presence of the advancing front can be observed in the middle of the IL-5 rock. However, from then on, the difference in permeability and porosity means that the advancing front takes a preferential path and gradually disappears until it reaches the end of the sample.

After 4.14 PVI of water, the water saturation is 0.692, and the residual oil saturation is 0.308. The endpoint of water injection and the starting point to begin oil injection (draining) until irreducible water saturation is reached again. Table 13 presents the oil injection results. During this process, 25 acquisitions were performed with X-ray computed tomography, and 6.9 PVI were injected. The flow rate varied from 0.2 to 0.3 ml/min during second oil injection. The oil saturation obtained was equal to 0.46, and the irreducible water saturation was equal to 0.54; these values are the same as those observed in the first oil saturation. Finally, the breakthrough time obtained during drainage was equal to 0.19 PVI, slightly higher than during water injection.

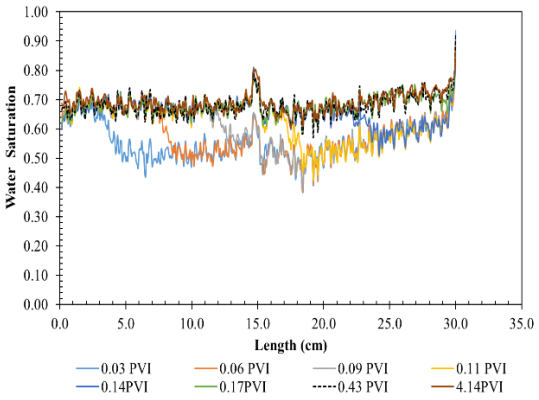

Fig. 10. Water saturation profile during brine injection until reaching Sor.

Table 12. Results of Brine injection (Imbibition) in Sample IL-5.

N° SCAN	Pore Volume Injected (PVI)	$\bar{S}_o$	$\bar{S}_w$
CT0		0.460	0.540
CT1	0.03	0.443	0.557
CT2	0.06	0.418	0.582
CT3	0.09	0.397	0.603
CT4	0.11	0.375	0.625
CT5	0.14	0.346	0.654
CT6	0.17	0.320	0.680
CT7	0.19	0.321	0.679
CT8	0.21	0.321	0.679
CT9	0.24	0.318	0.682
CT10	0.26	0.322	0.678
CT11	0.31	0.314	0.686
CT12	0.38	0.319	0.681
CT13	0.43	0.319	0.681
CT14	0.53	0.319	0.681
CT15	0.61	0.323	0.677
CT16	0.70	0.321	0.679
CT17	0.79	0.321	0.679
CT18	0.93	0.324	0.676
CT19	1.12	0.323	0.677
CT20	3.21	0.318	0.682
CT_{Final}	4.14	0.308	0.692

Figure 11 shows the oil saturation profile during the drainage process. However, the advance front can only be observed in the first two injected volumes. After 0.19 PVI, the breakthrough was reached. At this point, the advance front disappeared completely, and the oil saturation increased slightly, reaching 0.54.

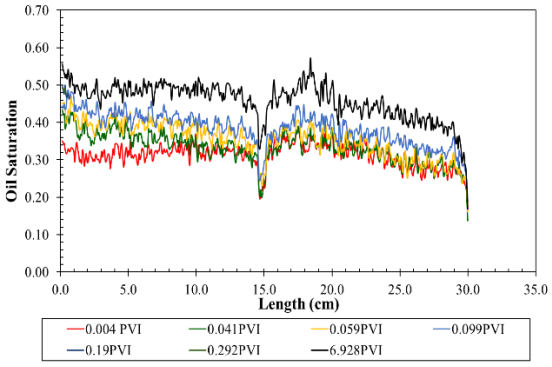

Fig. 11. Oil saturation profile during oil injection (drainage) until reaching S_{wi}.

Table 13. Results of Oil injection (Drainage) in Sample IL-5.

N° SCAN	Pore Volume Injected (PVI)	$\bar{S}_o$	$\bar{S}_w$
CT0		0.308	0.692
CT1	0.004	0.313	0.687
CT2	0.041	0.333	0.667
CT3	0.059	0.355	0.645
CT4	0.081	0.375	0.625
CT5	0.099	0.385	0.615
CT6	0.117	0.392	0.608
CT7	0.135	0.398	0.602
CT8	0.154	0.406	0.594
CT9	0.172	0.408	0.592
CT10	0.190	0.413	0.587
CT11	0.209	0.414	0.586
CT12	0.229	0.419	0.581
CT13	0.252	0.425	0.575
CT14	0.272	0.427	0.573
CT15	0.292	0.430	0.570
CT16	0.311	0.432	0.568
CT17	0.331	0.438	0.562
CT18	0.351	0.439	0.561
CT19	0.371	0.439	0.561
CT20	0.390	0.441	0.559
CT21	0.421	0.443	0.557
CT22	0.440	0.445	0.555
CT23	0.469	0.443	0.557
CT24	0.630	0.448	0.552
CT_{Final}	6.928	0.459	0.541

3.7 Absolute, effective and relative permeability measures

Initially, porosity and permeability measurements were performed on IL-3, IL-5, and IL-12 rock samples. During the displacement test, the absolute water permeability was measured, and the effective oil permeability in the S_{wi} and the effective water permeability in the S_{or} in the IL-5 sample were possible. Furthermore, the terminal points of the relative permeability curve during water injection (imbibition) and oil injection (drainage) were determined. The different permeability measurements were determined in different positions of the sample, as described in Figure 12, since the core holder has six pressure taps for measuring the differential pressure, of which five pressures were used during the sample displacement test. IL-5.

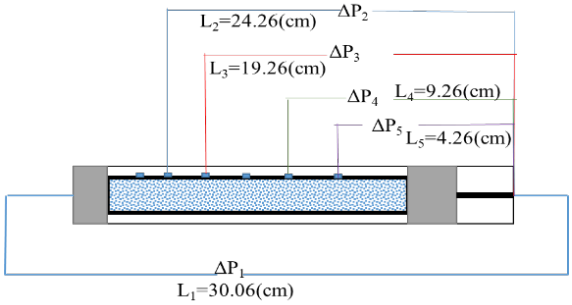

Fig. 12. Descriptive diagram of the position of the pressure taps along the IL-5 sample.

The different permeabilities measured during the displacement test are presented in Table 14.

Table 14. Absolute, effective, and relative permeability results of the IL-5 sample.

ΔP	k (md)	k_{abs}(md)	k_o @ S_{wi} (md)	k_{ro} @ S_{wi}
1	171.1	171.9	156.1	0.91
2		218.2	179.08	0.82
3		222.9	205.39	0.92
4		190.3	147.24	0.77
5		181.2	127.72	0.70
ΔP	**k_w @ S_{or} (md)**	**k_{rw} @ S_{or}**	**k_{o2} @ S_{wi} (md)**	**k_{ro2} @ S_{wi}**
1	3.76	0.0218	158.88	0.92
2	4.19	0.0192	177.75	0.81
3	4.7	0.0211	206.55	0.93
4	3.41	0.0179	149.44	0.79
5	3.19	0.0176	128.78	0.71

The permeability measured with the gas permeability meter and the absolute water permeability present a difference of approximately 0.5%. Four permeability values were also determined at different positions of the sample, from which it can be concluded that the sample presents a difference of approximately 13% between the permeabilities measured near the inlet (k_2 and k_3) and those measured near the outlet (k_4 and k_5). The effective permeability of the oil in the S_{wi} presented a value of 156.10 md during the first oil injection. After the second oil injection, a slight difference of approximately 1.78% was observed. However, the measurements between the inlet and outlet pressure tap presented a difference of 0.5 % to 1.5 %. The effective water permeability is 3.76 md at a residual oil saturation of 0.308, which is low permeability but coherent concerning the presence of a high S_{wi} (0.64) and S_{or} (0.308).

4 Conclusions

Among the presented and discussed results, we can highligh the following conclusions:

- The acquisition protocol applied in this study needs to be significantly improved in the case of low energy scan.
- The meticulous selection of the dopant underscored the study precision in quantity and type. This careful selection process contributed to our results accuracy and holds promise for practical applications in various scenarios.
- Our study employed different techniques to calculate porosity and permeability, observing significant variations between them. This observation deepens our understanding of the fluid dynamics and porous media and opens avenues for further exploration and refinement of those techniques.
- The B50s kernel was selected as the best reconstruction protocol for two-phase displacement for the acquisition protocol present in this work.
- Terminal points of the oil injection and water injection relative permeability curves were determined sucesfully.
- It was observed that when the decision matrix presents Δ values approximately equal, the cause is the significant difference in the CT number of the fluids (approximately 1000 HU) such as between brine and N_2. Based on this, it can be concluded that the fluids have approximately 1000 HU difference between the CT numbers. It is possible to use any acquisition and reconstruction protocol.

"We gratefully acknowledge the support and sponsorship by Equinor Brazil (Project ANP 23271-0). We also acknowledge the support of ANP (Brazil's National Oil, Natural Gas and Biofuels Agency) through the R&D levy."

References

1. Akin, S. & Kovscek, A. R. *Geological Society, London, Special Publications*, v. **215**, n. 1, p. 23-38, (2003).
2. Wellington, S. L., & Vinegar, H. J. *Journal of petroleum technology*, **39**(08), 885-898, (1987).
3. Withjack, E. M. *SPE formation evaluation*, **3**(04), 696-704 (1988).
4. Larmagnat, S., Des Roches, M., Daigle, L. F., Francus, P., Lavoie, D., Raymond, J., Malo, M, Aubiès-Trouilh, A. *Marine and Petroleum Geology*, **109**, 361-380, (2019).
5. Chaves, J. M. P., & Moreno, R. *Spe Journal*, **26**(1): 206–219, (2021).
6. Vaz, C. M. P., Tuller, M., Lasso, P. R. O., & Crestana, S. *Application of soil physics in environmental analyses: Measuring, modelling and data integration*, p.261-281, (2014).
7. Siddiqui, S., & Khamees, A. A. *In SPE Annual Technical Conference and Exhibition*, (pp. SPE-90520), (2004).
8. Fitzhenry, E., Martel, R., Robert, T., & Des Roches, M. *Colloids and Surfaces A: Physicochemical and Engineering Aspects*, **645**, p.128955, (2022).
9. Clinckspoor, K. J., Ferreira, V. H. S., & Moreno, R. B. Z. L. *CT&F-Ciencia, Tecnología y Futuro*, **11**(1), p.123-135, (2021).

10. Völgyes, D., Pedersen, M., Stray-Pedersen, A., Waaler, D., & Martinsen, A. C. T. (2017). *Journal of computer assisted tomography*, 41(1), 75-81, (2017).
11. Vargas, Janeth A. V. *University of Campinas (UNICAMP) Doctoral thesis* (2015). [sn].
12. Avizo3D. Version Pro 2023.1. *Thermo Fisher Scientific*, (2023).
13. Freire-Gormaly, M., Ellis, J. S., MacLean, H. L., & Bazylak, A. *Oil & Gas Science and Technology–Revue d'IFP Energies nouvelles*, ***71***(3), 33, (2016).